Available online at www.sciencedirect.com
ScienceDirect
Journal of the European Ceramic Society 31 (2011) 1619–1630
www.elsevier.com/locate/jeurceramsoc

Origin of light scattering in ytterbium doped calcium fluoride transparent ceramic for high power lasers

Andréas Lyberis [a], Gilles Patriarche [b], Patrick Gredin [a], Daniel Vivien [a], Michel Mortier [a,*]

[a] *Laboratoire de Chimie de la Matière Condensée de Paris, UMR-CNRS 7574, Chimie ParisTech, Université Pierre et Marie Curie, 11 rue Pierre et Marie Curie, 75231 Paris CEDEX 05, France*
[b] *Laboratoire de Photonique et de Nanostructure, UPR20 CNRS, Route de Nozay, 91460 Marcoussis, France*

Received 30 July 2010; received in revised form 21 February 2011; accepted 28 February 2011
Available online 1 April 2011

Abstract

The origin of light scattering defects was studied in transparent 6 at% Yb:CaF_2 ceramics. Samples were synthesized by a soft chemistry route followed by sintering and hot pressing which leads to highly transparent ceramics with low scattering losses (0.016 cm^{-1} at 1200 nm). Light scattering defects were studied using scanning transmission electron microscopy (STEM) and high angle annular dark field-STEM (HAADF-STEM) techniques. Energy dispersive X-ray spectroscopy showed a 50% increase in Yb^{3+} concentration at grain boundaries. A 3–5 nm thick oxygen rich phase was detected at some grain boundaries by both HAADF-STEM and EDS. The origin of the oxygenized grain boundaries was traced to a 2–15 nm thick oxygenized shell present on the starting powders. Analysis of high resolution HAADF-STEM images revealed that Yb^{3+} substitutes into the fluorite lattice as clusters rather than individual ions, but the types of clusters could not be identified by this imaging technique.

Keywords: CaF_2; Ytterbium; Optical properties; Hot pressing; Grain boundaries; Defects

1. Introduction

Transparent ceramics are materials for solid state lasers, which may challenge single crystals and glasses. Compared to single crystals, transparent ceramics have three main advantages: higher thermal shock parameter and fracture strength, increase scalability and absence of macroscopic segregation of the dopant during the process. Compared to glasses, ceramics have a drastically higher thermal conductivity. A large range of oxide laser ceramics has already been synthesized.[1] The most studied material, with outstanding laser properties, is yttrium aluminium garnet (YAG).[2] Continuous wave (cw) diode-pumped Nd:YAG laser ceramics have generated 1.46 kW with 42% slope efficiency[3] and 67 kW at the Lawrence Livermore National Laboratory (LLNL).[4] Recently, continuous wave output power densities of 3.9 kW cm^{-2} and 0.19 MW cm^{-3} have been achieved with ytterbium doped YAG.[5]

Compared to oxides, fluoride compounds such as calcium fluoride CaF_2 (fluorite) and strontium fluoride SrF_2 have wider optical transparency (from vacuum UV up to 7 μm), lower phonon frequency cut off (495 cm^{-1} for CaF_2[6] compared to 830 cm^{-1} for YAG[7]) as well as lower linear and non-linear refractive indexes. Fluorides allow laser oscillation with high optical efficiency leading to decreased thermal loading and simplified development of laser sources. Furthermore, the variation of the refractive index with the temperature *dn/dt* of these fluorides is negative,[8,9] whereas it is usually positive for oxides.[10] Therefore, the combination of oxides and fluorides appears to be an interesting way of designing high power lasers to avoid the thermal lensing effect.

The trivalent ytterbium, Yb^{3+}, is very attractive as a luminescent ion for laser application because it has a simple two multiplet electronic structure which avoids losses by cross relaxation or up-conversion. In addition, its low quantum defect

* Corresponding author. Tel.: +33 1 53 73 79 27; fax: +33 1 46 34 74 89.
E-mail addresses: andreas-lyberis@chimie-paristech.fr (A. Lyberis), gilles.patriarche@lpn.cnrs.fr (G. Patriarche), patrick.gredin@upmc.fr (P. Gredin), daniel-vivien@enscp.fr (D. Vivien), michel-mortier@chimie-paristech.fr (M. Mortier).

0955-2219/$ – see front matter © 2011 Elsevier Ltd. All rights reserved.
doi:10.1016/j.jeurceramsoc.2011.02.038

enables high lasing efficiencies, its broad absorption band facilitates diode pumping and its broad emission band is suitable for ultrashort laser pulse generation or laser wavelength tunability.[11]

For several years, our team has studied the processing of transparent laser ceramics of CaF_2:Yb^{3+}[12,13] because of its high thermal conductivity (9.7 $W\,m^{-1}\,K^{-1}$ for pure CaF_2 compared to 11.0 $W\,m^{-1}\,K^{-1}$ for pure YAG).[9] Several studies have recently shown strong interest in single crystal Yb:CaF_2 because of its laser characteristics[11]: tunable laser oscillation with 50% slope efficiency,[14] generation of ultrashort laser pulses (down to 150 fs)[15] and self-Q-switching.[16] Ytterbium doped CaF_2 also exhibits a higher damage threshold compared to ytterbium doped YAG (52 $J\,cm^{-2}$ and 16 $J\,cm^{-2}$ respectively for a 10 ns pulse duration and a center wavelength of 1064 nm).[17] Due to these characteristics, ytterbium doped CaF_2 appears as a very promising material for high power laser applications.

Recently, Basiev and co-workers prepared CaF_2–SrF_2–YbF_3 transparent ceramics by uniaxial hot pressing single crystals made by the Bridgeman process. These ceramics showed laser properties similar to those of a single crystal of the same composition.[18] The process used by Basiev and co-workers is similar to the one described in the very first paper about laser ceramics.[19] The present paper is devoted to the synthesis and the optical characterization of ytterbium doped CaF_2 transparent ceramics for high power laser applications obtained from powders synthesized by a soft chemistry route for the starting material and not from single crystals as in previous works.[18] Indeed, a process from powder synthesis to ceramic should be more appropriate for the production of transparent ceramics on a large scale and avoids the strong uniaxial character of the ceramics demonstrated by Basiev et al.

The studies presented here are particularly focused on the understanding of the origin of light scattering in the fluoride ceramics in order to improve their optical quality. We have already obtained ceramics with optical losses as low as 0.16 cm^{-1} at 1200 nm (corresponding to an in-line transmittance of 97.2%). However, this value has still to be decreased for efficient laser operation.

Scanning transmission electron microscope (STEM) studies of the YbF_3–CaF_2 powders and sintered ceramics show some defects such as higher ytterbium concentration at grain boundaries and, in some cases, of oxygen. These defects are thought to be responsible for the optical losses measured in our ceramics. There are only a few published accurate studies of grain boundaries in transparent ceramics that used confocal Raman and fluorescence spectroscopic imaging and high resolution TEM (HRTEM).[20,21] Up to now, high angle annular dark field STEM (HAADF-STEM) has been only used to study rare-earth distribution in silicon carbide[22] or in silicon nitride.[23,24] We present here the first study of grain boundaries in transparent laser ceramics with the HAADF-STEM mode where the resolution is nearly 1 Å as it can be seen in following high resolution images. In addition, chemical compositions have been measured with the available quantitative energy dispersive X-ray (EDX) analysis.

Furthermore, the high resolution electron microscopy that we have carried out shows that the distribution of ytterbium ions in the bulk ceramic does not occur randomly. Initially, Catlow has predicted, from theoretical simulations, the formation of ytterbium clusters[25,26] in ytterbium doped CaF_2 that have been confirmed later with spectroscopic techniques and have shown that these clusters correspond to the luminescent centers.[27] The work presented here reports, to our knowledge, the first direct imaging of these ytterbium clusters in the Yb^{3+}:CaF_2 ceramics.

2. Experimental

2.1. Synthesis

2.1.1. Nanoparticle synthesis

The nanoparticles were synthesized using commercially available products. Calcium nitrate (99.98%) was provided by Alfa Aesar and ytterbium nitrate (99.999%) by Aldrich. The hydrofluoric acid (HF(aq)) used was 48 wt% from VWR. The water was distillated prior use.

The chosen synthesis was coprecipitation of nitrates in HF(aq), which has previously been described.[12,13] The coprecipitation is based on the following reaction:

$$(1-x)Ca(NO_3)_2 + xYb(NO_3)_3 + (2+x)HF(aq) \rightarrow Ca_{1-x}Yb_xF_{2+x} + (2+x)HNO_3$$

where x is the doping level, varying from 0.25 to 10 at%.

The solubility of YbF_3 in the fluorite phase is known to be approximately 40 at%.[28,29] In these doping conditions, the ytterbium can be considered as totally soluble in the fluorite crystal structure.

A solution containing the cationic precursors was made by dissolving nitrate salts in distilled water. Then, this solution was added dropwise to the magnetically stirred HF(aq) solution, leading to the formation of Yb^{3+} doped CaF_2 nanoparticles according to the above chemical reaction. The obtained mixture was centrifuged at 13,000 rpm for 30 min. The resulting nanoparticles were then washed and centrifuged with distilled water several times before drying at 80 °C. The obtained powder was annealed at 400 °C under anhydrous argon atmosphere for 4 h.

2.1.2. Sintering protocol

Powder obtained by the coprecipitation method was pelletised by uniaxial pressing followed by cold isostatic pressing. The resulting disks of compacted powder were then sintered under vacuum better than 0.1 Pa at 600 °C for 1 h. The ceramics were finally hot pressed at 900 °C and 60 MPa under vacuum better than 0.1 Pa in a graphite die covered by an alumina powder layer to protect the ceramic from carbon contact.

2.1.3. Preparation for STEM observation

The studied material was observed with a transmission electron microscope (TEM) in thin section of the transparent ceramic and in powder form. The thin sections of ceramics are prepared

by focused ion beam (FIB) and some surfaces are polished with a precision ion polishing system (PIPS) Gatan (2.5 kV (2 min) then 2 kV (2 min) with an angle range from 5° to 8°). The thin sections of ceramics were deposited on a copper grid covered with carbon film (5–10 nm thick). For powder observation, the particles are grown by an annealing at 600 °C for 4 h under anhydrous argon atmosphere in order to facilitate their orientation in the TEM. To prepare powder samples for TEM, the powder was dispersed in ethanol under ultrasound and gathered on a copper grid covered with carbon film (5–10 nm thick).

2.2. Experimental techniques

Absorption spectra in the near IR and in the visible were performed on a Cary 6000i spectrophotometer on polished samples with surface roughness of λ/3 at 585 nm.

Transmission electron microscopy (TEM) was performed on a 200 kV Jeol 2200FS microscope with a spherical aberration corrector on the scanning transmission electron microscope (STEM) probe. The STEM-HAADF (high-angle annular dark-field) images are detected with a half angle of 100 mrad (inner detector angle) and 170 mrad (outer angle). The corrected convergence half angle of the STEM probe is 30 mrad and the probe intensity is 55 pA. The acquisition time is 38.7 s per image (1024 × 1024 pixels). We ensured that all TEM measurements and images were taken in the center of all samples by focusing on the top of the sample, then focusing on the bottom of the sample, and finally choosing an analysis depth between these two positions. The depth of focus of the TEM is 4 nm. The microscope was equipped with a quantitative energy dispersive X-ray (EDX) analyzer for chemical composition analysis. The precision of the measured atomic fraction was approximately 0.5 at%.

The STEM-HAADF probe signal is proportional to the square of the atomic number (Z^2). The contrast of the image was due to a difference in the chemical composition in a section of 4–5 nm thick due to the short depth-focus of the aberration-corrected STEM.[30] The larger the mean atomic number Z is, the brighter the zone will appear. Every atom in a column has the same contribution to the mean Z.[31,32]

3. Results and discussion

3.1. Optical characterization

We produced doped calcium fluoride ceramics with doping level varying from 0 to 10 at%. Our experiments showed that the optimal composition to achieve the best transparency (Fig. 1a) is close to 5 at% ytterbium doped CaF_2. Indeed, the undoped and 10 at% ytterbium doped ceramics are less transparent than the 5 at% one (0.86 compared to 0.19 cm^{-1} at 1200 nm for the 10 and 5%). The correlation between the ytterbium concentration and the ceramic transparency is under investigation and will be discussed in a forthcoming paper.

The transparency of the 5 at% ytterbium doped CaF_2 ceramic is characterized by optical absorption. From the measurement of this optical absorption we have distinguished two different sources of optical losses. The first source consists of the light reflection on the two material faces, which lightly depends on the doping level but is independent of the sample thickness. The second source of optical losses is due to the material itself and only depends on the sample thickness. The effect of the surface reflections has to be suppressed to allow comparison between the different ceramic samples. The light reflections on the faces can be removed by depositing an anti-reflection coating or by subtracting the reflection losses from the measured data. The latter method has been chosen and a corrected absorption coefficient α_{corr} is calculated according to Eq. (1) where multiple reflections are neglected:

$$\alpha_{corr} = -\frac{2.3}{\varepsilon} \log\left(\frac{10^{(-OD)}}{(1-R)^2}\right) \quad (1)$$

with:

$$OD = \log\left(\frac{1}{T}\right) \quad (2)$$

$$R = \left(\frac{n_1 - n_2}{n_1 + n_2}\right)^2 \quad (3)$$

$$T = (1-R)^2 \exp(-\alpha_{corr}\varepsilon) \quad (4)$$

where OD is the optical density, T is the transmittance, ε is the sample thickness and R is the reflectance per face.[33] n_1 is the refractive index of the first media of the interface, air for example with $n_{air} = 1$, and n_2 is the refractive index of the second medium, fluorite, calculated using the Sellmeier dispersion equation with the Sellmeier coefficients reported in Ref. 8. At 1200 nm, the refractive index for an undoped CaF_2 single crystal is 1.4277 and the reflectance per face (R) is 3.10%.

Fig. 1b shows the reflection adjusted optical absorption of a 1.74 mm thick 5 at% Yb:CaF_2 ceramic and a 2 mm thick undoped CaF_2 single crystal. The ceramic exhibits the characteristic Yb^{3+} absorption band in a CaF_2 lattice between 900 and 1050 nm due to the $^2F_{7/2}$ to $^2F_{5/2}$ transition.[34–36] Yb^{2+} has a characteristic absorption near 350 nm which is not present in Fig. 1b, thus Yb exists primarily as Yb^{3+} in the lattice.[37–39] The single intense absorption band at 220 nm of our ceramic has to be the signature of oxygenized phase among the material. The origin and the effects of oxygen will be discussed further in this paper.

The low level of optical losses cannot be neglected (0.16 cm^{-1} compared to 0.02 cm^{-1} for the reference, at 1200 nm). There is also an important increase of the absorption coefficient towards short wavelengths due to the defects of the sample. The polishing of the sample surface (microroughness of λ/3 at 585 nm) is supposed to be good enough to neglect the losses induced by surface roughness. The understanding of the origin of these losses has been studied with electron microscopy to identify structural defects which generally consist of three types of scattering sources in a polycrystalline material: pores, secondary phases and grain boundaries.[28,29] Now, we will focus on the structural study to understand the presence of each type of scattering source.

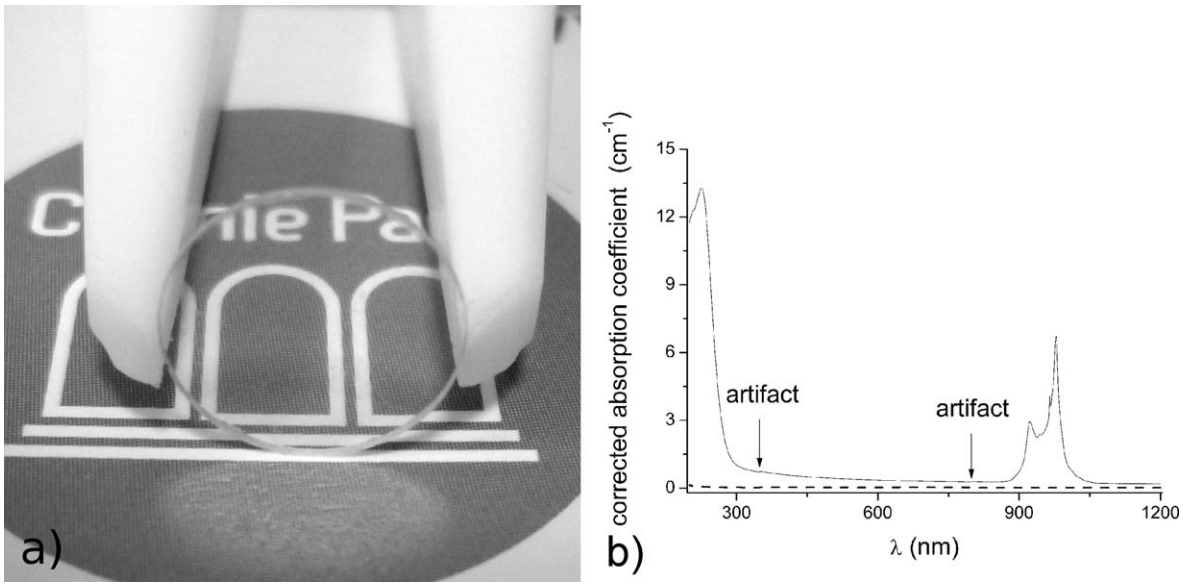

Fig. 1. (a) Photograph of the transparent ceramic of CaF_2: 5 at% Yb, (b) corrected absorption coefficient spectra of the CaF_2:5 at% Yb ceramic, in solid line, and of an undoped single crystal window of CaF_2, in dashed line (artifacts are due to the spectrometer detector and source).

3.2. Grain scale homogeneity

The presence of pores and secondary phase grains has been studied by STEM. The contrast of the bright field STEM (BF-STEM) images is mainly due to the different orientations of the grains whereas the contrast of the high angle annular dark field STEM (HAADF-STEM) images is due to local chemical composition. The STEM images presented in Fig. 2 show no porosity in the ceramic which has an average grain size of 500 nm. The homogeneity of the HAADF image (Fig. 2b) confirms the homogeneity of the chemical composition and excludes the presence of secondary phase grains or large cavities at the grain boundaries. The remaining scattering sources are the grain boundaries.

3.3. Grain boundaries

In our ceramics, we have identified two types of defects localized at grain boundaries. One with ytterbium segregation, representing nearly 90% of the grain boundaries and another one with oxygenized grain boundary phase representing the remaining 10%, with none or only a few ytterbium ions. They are considered separately.

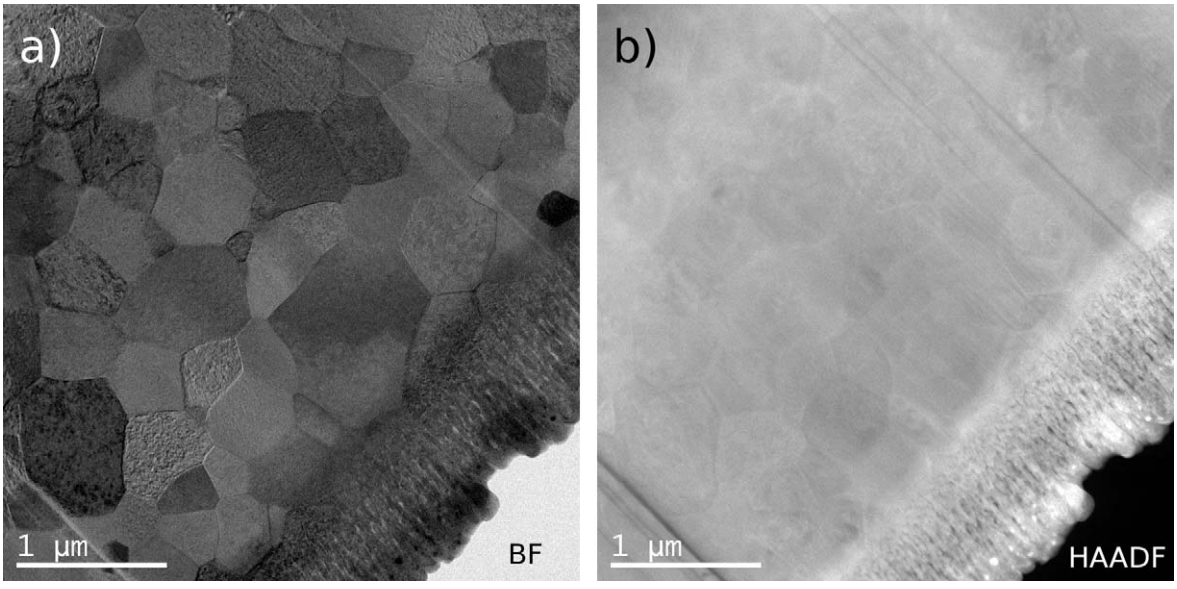

Fig. 2. STEM images (a) bright field and (b) HAADF of a thin section of a transparent ceramic of CaF_2:6.4 at% Yb prepared by focused ion beam (FIB). The right lower corner zone has been damaged during the focused ion beam (FIB) process.

3.3.1. Ytterbium segregation

The doping level of the synthesized powders is smaller than 10 at% and in the studied ceramic, the ytterbium atomic fraction does not exceed 9%. Under these doping conditions, the ytterbium can be considered as totally soluble in the fluorite crystal structure because its solubility in the fluorite phase reaches 40 at%.[39,40] In the following studies, the theoretical ytterbium atomic fraction in the studied ceramic is 6.4 at%; this atomic fraction is close to the optimal one described before.

Chemical profiles measured on several grains by EDX analysis have been drawn on the HAADF-STEM image in Fig. 3a. The measured ytterbium atomic fraction reported in Fig. 3b shows three main peaks (labeled 1, 2 and 3) which correspond to the three grain boundaries along the profile (labeled 1, 2 and 3 in Fig. 3a) and which exhibit a higher ytterbium concentration than the mean level. This analysis underlines a segregation of the ytterbium at the grain boundaries, 7–9 at% of ytterbium instead of an average 6.3 at% measured on the grains. A higher spatial resolution EDX analysis of the ytterbium segregation across a grain boundary is shown in Fig. 3c. This analysis highlights the segregation of the rare earth ions in a 25 nm thick region (labeled 4 in Fig. 3a) centered on the grain boundary (the EDX profile is presented in Fig. 3c). This region does not correspond to a secondary phase or precipitates fixed at the grain boundary but to an increase of the ytterbium incorporation in the calcium fluoride phase.

In the HAADF-STEM image Fig. 4a, the grain boundary shows a brighter zone which corresponds to a segregation of ytterbium ions. The long range atomic ordering of the fluorite crystal structure is preserved as far as the grain boundary despite a local higher amount of dopant (Fig. 4 images) suggesting that there is no secondary phase at the grain boundary which is almost perfect. These photos show images of grain boundaries with the best resolution because images of this ceramic with atomic resolution could not be performed due to the electrical insulating property of the fluorite. In order to reach a higher resolution, the grain boundary study has been carried out on powders because the huge specific area of the nanometric powder decreases the charging effect on the studied sample. Some of the particles have been sintered and present grain boundaries due to the applied thermal treatment (see below Section 4).

Fig. 5 is a HAADF-STEM image where a spot corresponds to an atomic column in the images of 4 nm deep which corresponds to the field depth of the microscope. The ytterbium segregation can also be observed in a powder at very low doping level, e.g. 0.5 at% of ytterbium. The greater the atomic number is, the brighter the atom appears on the HAADF-STEM image. The grain boundary shown in Fig. 5 appears clearly brighter than the regions inside each grain indicating unambiguously the segregation of ytterbium ions at the grain boundary. Another particularity of this image is the long range atomic ordering of the fluorite crystal structure preserved as far as the grain boundary in the two grains. Some previous works have shown that the segregation of the dopant is governed by the minimization of the interfacial energy, depending on the direction of the surface, which minimize also the one of the bulk/interface system.[41,42] Thus, the equilibrium concentration of the rare earth at the grain

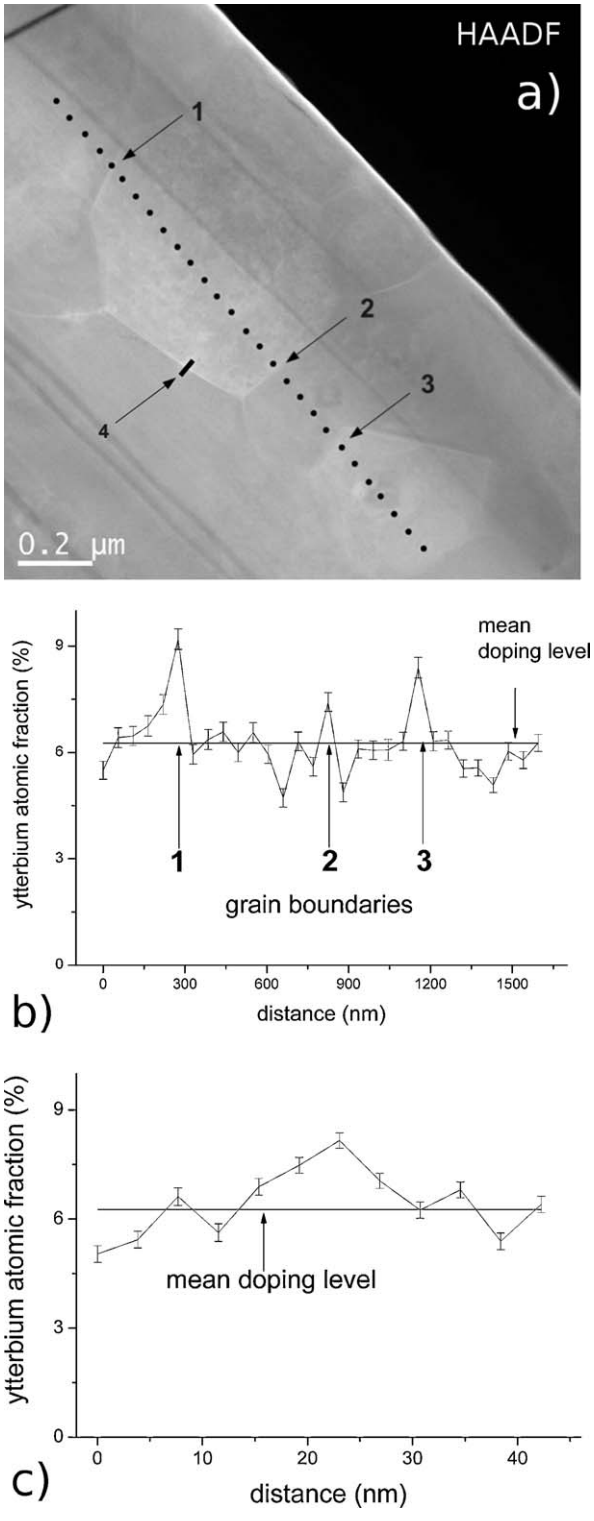

Fig. 3. (a) HAADF-STEM image of a transparent ceramic of CaF_2:6.4 at% Yb prepared by FIB where dots and rectangle represent the location of the EDX analyses, (b) EDX profile along the dots over several grains, (c) EDX profile across the grain boundary labeled 4 in Fig. 3a. The volume of material analyzed depends on the sample thickness (about 100 nm) and the geometry of the probe (in particular the angle of convergence). For each point, the maximum diameter of the cone of material probed is approximately of 1.5 nm.

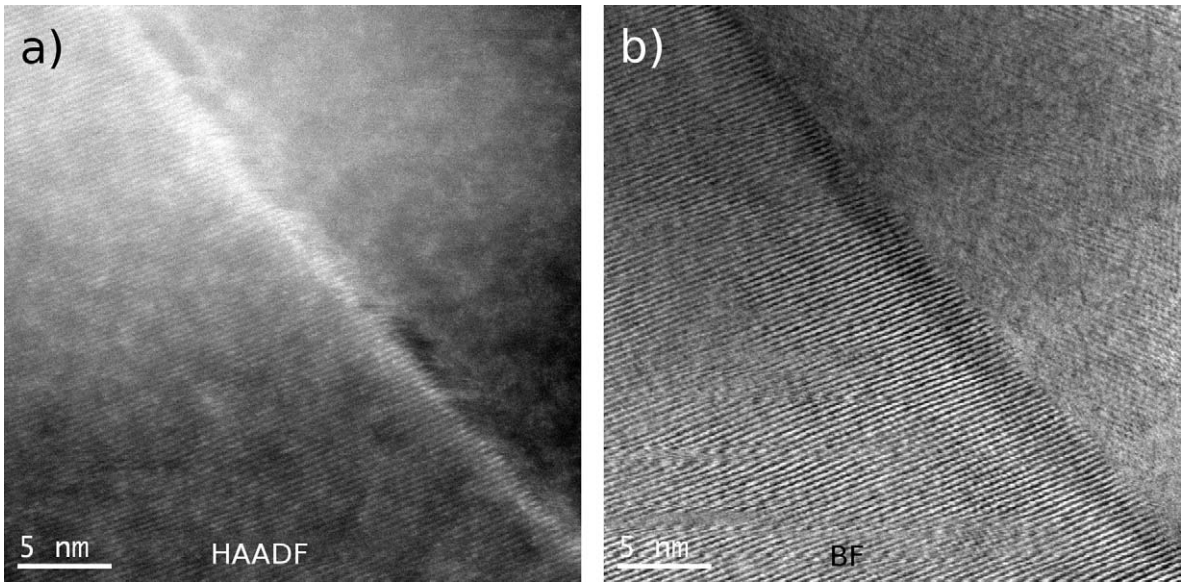

Fig. 4. STEM images (a) HAADF (b) bright field of a grain boundary in a transparent ceramic of CaF_2:6.4 at% Yb prepared by FIB with precision ion polishing system (PIPS) treatment showing long range atomic ordering between two grains with ytterbium segregation at the grain boundaries.

boundary depends on the bonding environment and the facility of the crystal structure to incorporate the rare earth ions, which is higher close to the surface than in the bulk. Indeed, the deformation of the lattice induced by the dopant can be greater close to the surface without a destruction of the crystal structure. This particular structure is a twin-boundary corresponding to a rotation of 49.5° (±0.2°) around the [1 1 0] zone axis, which is the common axis at two single crystals in contact.

3.3.2. Oxygenized grain boundaries

The HAADF image presented in Fig. 6a shows the presence of a darker region corresponding to a grain boundary phase. The brightness of this phase is very low indicating a lower mean square atomic number (Z^2) and probably a lower content of ytterbium compared to the one observed inside the grain. On the BF-STEM images given in Fig. 6b, this region appears as amorphous or not in diffraction condition. EDX measurements of this grain boundary phase show a high concentration of oxygen. Therefore, this region corresponds to a different phase, characterized by a different chemical composition, observed sometimes at the grain boundary. The presence of oxygen in some of the grain boundaries of the ceramic is unexpected in a fluorite structure. Indeed, calcium fluoride is the least hygroscopic compound of all fluorides and its solubility in water is very low, $pK_s \sim 10$.[43]

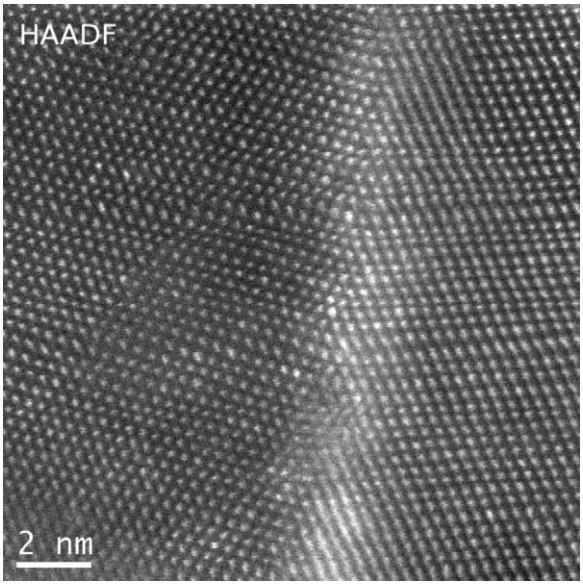

Fig. 5. HAADF-STEM image of ytterbium segregation at the grain boundary in CaF_2:0.5at% Yb powder along the [2 1 1] zone axis of the crystal of the left side from the twin boundary.

Investigations on powders have been performed in order to understand the origin of the oxygen among the ceramic. An EDX analysis has been performed on a single particle (Fig. 7a) along a straight line which underlines the difference of O/(O + Ca) and F/(F + Ca) ratios. The EDX profile is plotted in Fig. 7b. In Fig. 7c, a crystallized shell containing oxygen can be observed at the surface of the particle. This type of oxygenated shell has also been observed in the 0.5 and 10 at% ytterbium doped powder. The doping level has no effect on the presence of this shell. The EDX profile shows the important O/(O + Ca) ratio at the surface of the particles (60 at%), which is in good agreement with the calcium hydroxide $Ca(OH)_2$ composition. It can also be noted that the ytterbium concentration in the shell is very low, close to zero. The measured oxygen concentration does not reach zero even in the bulk of the powder particle because the EDX analysis integrates the chemical composition of the whole sample thickness and therefore of the outer shell.

These EDX measurements highlight the presence of calcium hydroxide ($Ca(OH)_2$) and not only of CaO. CaO is known to be unstable in water or in a moist atmosphere and it is formed by the decomposition of $Ca(OH)_2$ above 500 °C in air.[44] Therefore, the $Ca(OH)_2$ that might have been formed during the synthesis will

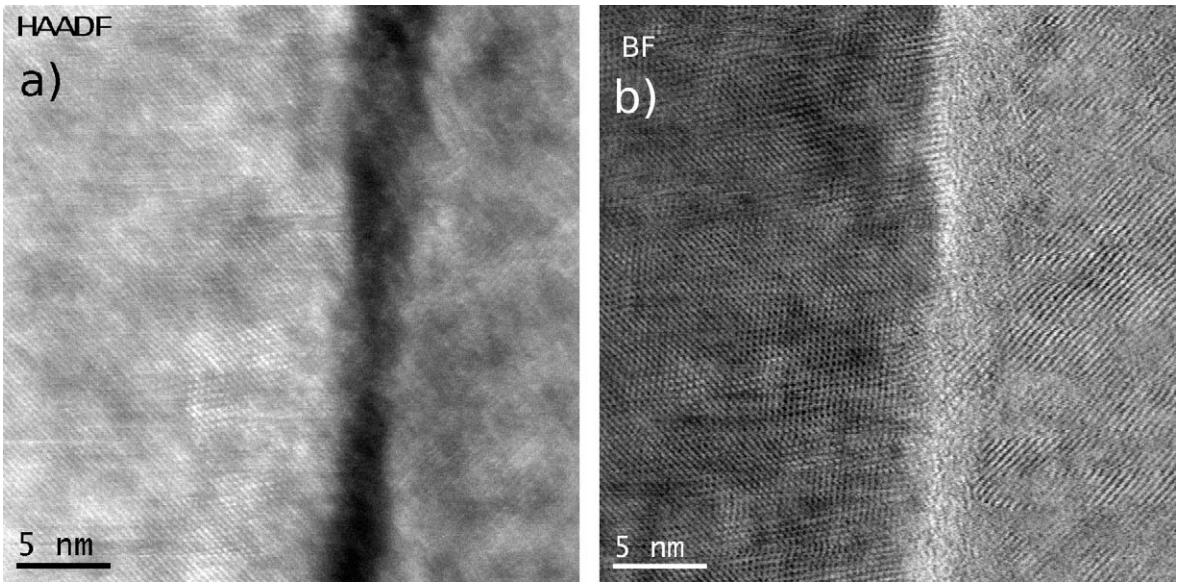

Fig. 6. STEM images (a) HAADF, (b) bright field showing a grain boundary secondary phase amorphous or out of diffraction conditions in a transparent ceramic of CaF_2:6.4 at% Yb prepared by FIB.

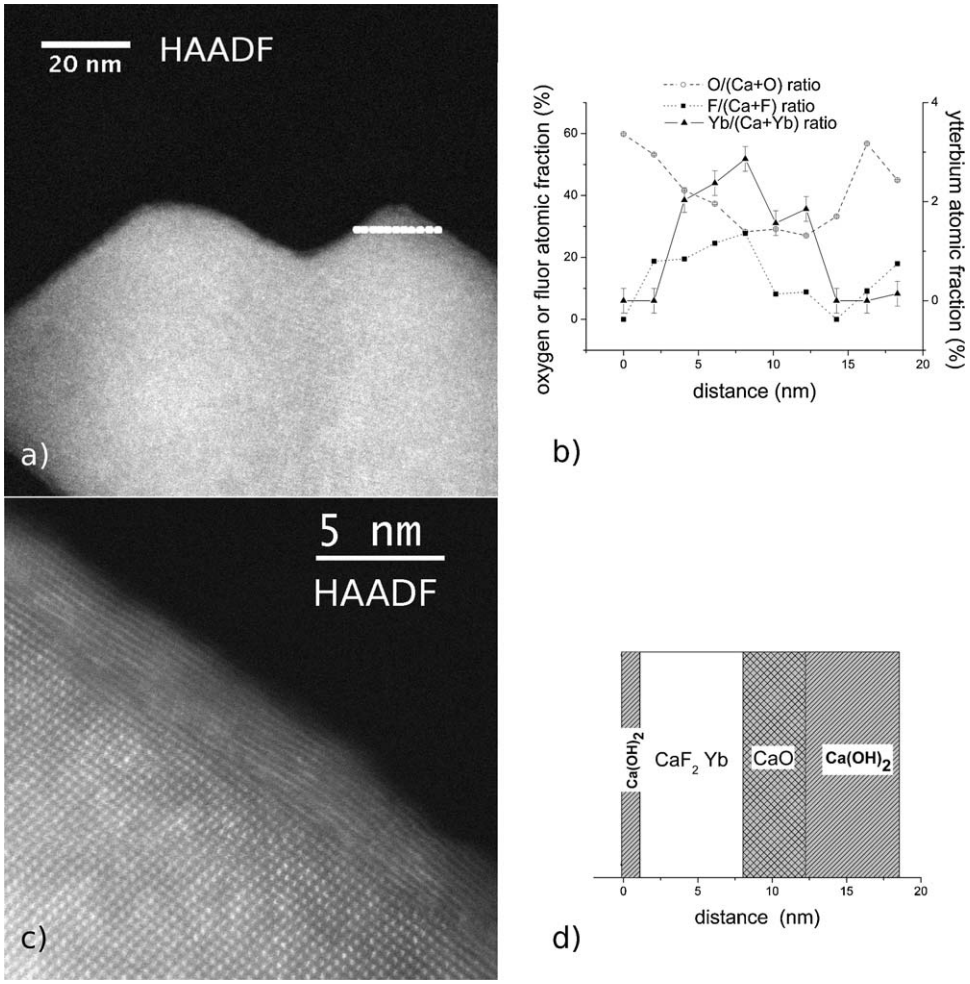

Fig. 7. (a) HAADF-STEM image of a CaF_2:5 at%Yb powder particle with EDX analysis of the shell composition, (b) EDX profile with Yb/(Yb + Ca) ratio (solid line), O/(O + Ca) ratio (dashed line) and F/(F + Ca) ratio (doted line), (c) HAADF-STEM image of the shell of the same particle and (d) schematic view of the composition along this profile.

not be decomposed into calcium oxide during the annealing step (400 °C for 4 h under argon atmosphere) described in Section 2.

The simplified diagram given in Fig. 7d is a schematic view of the composition along the measured EDX profile. We can observe two types of surfaces: one very thin shell only composed of $Ca(OH)_2$ and a thicker one itself made up of two layers stacked on each other, one layer of CaO and another layer of $Ca(OH)_2$. These two different types of shell could be the source of the different types of grain boundaries observed in the ceramic. Grain boundaries with ytterbium segregation could be formed by sintering particles with thin calcium hydroxide shell where ytterbium atoms are situated close to the surface. Indeed, if the oxygenized shell is thin enough, it could not be considered as a barrier for the fluorine diffusion. The oxygen could also migrate too and would finally be diluted in the fluorite lattice. On the contrary, the grain boundaries with oxygen are more likely to be formed by two particles with thick oxygenized shells that could be considered as a barrier for the fluorine diffusion and lead to the formation of an oxygenized grain boundary phase (Fig. 6).

TEM analysis of many grain boundaries and particle surfaces reveals that the oxide and hydroxide layers are non-uniform. The non-uniformity of the powder surfaces can be seen in the chemical analysis and TEM images of the two powder surfaces in Fig. 7a. The surface layer for an individual particle may be affected by the crystallographic plane of the nanoparticle surface as well as trace element (ppm level) impurities that may be present at the particle surfaces. Further, the particle surface layer thickness and chemistry may be altered during drying, annealing and sintering. This can lead to significantly smaller amounts of oxygen/hydroxyls present in the ceramic than would be predicted by looking at the TEM data for a single nanoparticle. Thus it is not possible to make quantitative predictions about the oxygen content of the sintered ceramic from the particle surface analysis.

It is interesting to note that oxygen was detected at only a fraction of the grain boundaries in the ceramic. There has been recent work[45] showing that specific grain boundaries may locally stabilize grain boundary phases, and that a single ceramic sample may contain several different types of grain boundary phases. It is therefore reasonable that some of the grain boundaries contain an oxygen rich phase, while others do not. At this point, the precise reasons that a specific boundary stabilizes a specific grain boundary phase are unclear, but it may be a function of local chemistry and grain boundary parameters (misorientation, grain boundary surface energy, etc.)

3.3.3. Influence on the optical absorption

So, we have identified two types of defects located at the grain boundaries in our ceramics. One with ytterbium segregation and fluorite crystal structure continuity (Fig. 4) and another one with an oxygenized grain boundary phase with none or only a few ytterbium ions (Fig. 6). Moreover, we have identified that the oxygen among the ceramic is brought in the process during the powder synthesis before the sintering. The studied fluoride ceramics have only inhomogeneities of grain boundaries as source of optical losses whereas porosity in oxide ceramics, such as yttrium aluminium garnet (YAG), also represents a major source of optical losses.

Table 1
Refractive indexes for different compounds.

	Compound	n evaluated at 500 nm	References
a	CaF_2:6.4 at% Yb	1.447	This work
b	CaF_2:9 at% Yb	1.453	This work
c	CaF_2	1.434	[49]
d	YbF_3	1.56	[50]
e	CaO	1.871	[51]

The refractive index is very different in CaF_2 and in CaO because of the different ionicity of the material. The Gladstone and Dale rule[46] applied to minerals has been used to evaluate the refractive index of the bulk material, of a grain boundary with ytterbium segregation and of an oxygenized grain boundary.[47]

$$K_{GD} \quad (\text{solid solution}) = \sum w_i K_{GD}(I) \tag{5}$$

$$K_{GD}(I) = \frac{n(I) - 1}{d(I)} \tag{6}$$

where $n(I)$ is the refractive index of the compound I, $d(I)$ its density, w_i its weight fraction in the solid solution and K_{GD} is the specific refractive index of the material.

The specific refractive index of some oxides and some fluoride compounds have been calculated[48,49] and we used them to estimate the refractive indexes of doped material with Eqs. (5) and (6) given in Table 1(a and b) together with the known refractive index of pure compounds (c, d and e). With the estimated refractive indexes, the reflectance R at different grain boundaries has been evaluated with Eq. (3). They are reported in Table 2 and they indicate that the reflectance at an oxygenized grain boundary is 4000 times the reflectance of a grain boundary exhibiting an ytterbium segregation. Therefore, the main scattering source is oxygenized grain boundary phases and not segregation of ytterbium at the grain boundaries.

The oxygenized secondary phases at the grain boundaries of the ceramic can be considered as the source of the 0.16 cm^{-1} residual losses measured in our ceramic at 1200 nm. There remains an absorption band at 220 nm (Fig. 1b) that cannot be attributed to Yb^{2+} absorption in a CaF_2 lattice because there should be a second intense absorption band at 350 nm in this case. A 190 nm absorption band corresponds to a simulated charge transfer between oxygen and rare-earth ions in the Yb^{3+} doped $Lu_2Si_2O_7$ oxide.[52] This kind of charge transfer between ytterbium and oxygen can occur in our calcium fluoride ceramics because of the presence of some oxygenized grain boundary phases that could explain the observed band at 220 nm. This

Table 2
Evaluated reflectance for grain boundaries with ytterbium segregation or oxygenized secondary phase.

Grain boundary composition	R evaluated at 500 nm
6.4–9 at% CaF_2 6.4 at% Yb–CaO	0.0004% 1.63%

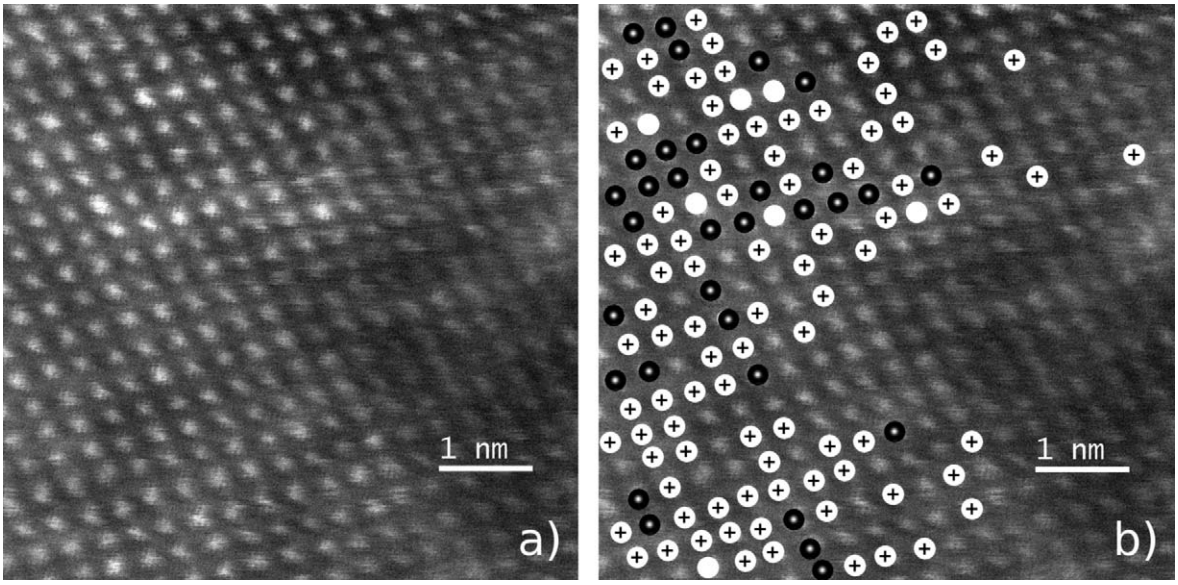

Fig. 8. (a) HAADF-STEM image with [1 1 0] zone axis of CaF_2:5 at% Yb powder particle presenting an inhomogeneous distribution of the ytterbium ions, (b) same image with ytterbium localization using dots (white disk with black cross, black disk with white point and white disk for one, two and three ytterbium ions respectively). The dark zone at the right lower corner corresponds to a thinner zone induced by the sample preparation.

absorption band is not observed with the same intensity in every sample and does not depend on the doping level. These different intensities can be attributed to small amounts of ytterbium ions randomly distributed in the oxygenized grain boundary phases mainly composed of pure CaO. CaF_2 has a measured electronic gap of 12.1 eV[53] corresponding to an absorption threshold of 103 nm while the CaO has an electronic gap of 7.1 eV[54] corresponding to a calculated absorption threshold at 175 nm that cannot be considered as the origin of the 220 nm absorption band. The increase of the light absorption below 300 nm in the calcium fluoride ceramics can be therefore a convolution of the charge transfer band Yb–O with the beginning of the absorption threshold due to the CaO gap. As a conclusion, the increase of the light absorption below 300 nm and the band observed at 220 nm indicate the presence of CaO inside our CaF_2 ceramics.

3.4. Ytterbium clusters

The study of ytterbium distribution between the grain and the grain boundary has shown a clustering effect of the ytterbium ions in the CaF_2 lattice.

The HAADF images of ytterbium doped powders Figs. 8a and 9a exhibit a non-random distribution of ytterbium ions in the columns. Moreover, the brightness is the sum of the contribution of all atoms in the column of 4 nm. The brightness of a column with ytterbium ions will be higher than a column

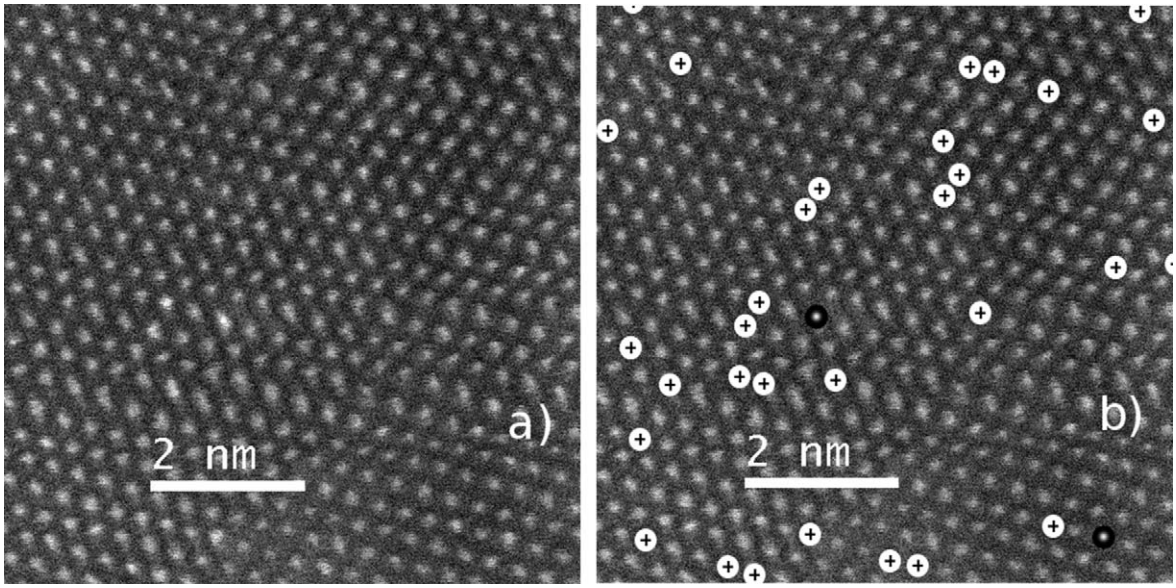

Fig. 9. (a) HAADF STEM image with [1 1 0] zone axis of CaF_2:0.5 at% Yb powder particle exhibiting an inhomogeneous distribution of the ytterbium ions, (b) same image with ytterbium localization using dots (white disk with black cross, black disk with white point for one and two ytterbium ions respectively).

with only calcium ions because the contrast of the HAADF-STEM mode is theoretically proportional to the mean square atomic number (Z^2) of the column. Using this characteristic, columns with ytterbium ions have been marked in the HAADF images (Figs. 8b and 9b) with dots (white disk with black cross, black disk with white point and white disk for one, two and three ytterbium ions respectively).

A 5 at% doped powder is composed of 1 ytterbium ion for 19 calcium ions which is too high to identify a precise cluster geometry. A 0.5 at% powder has been used for this study. The [1 1 0] zone axis HAADF-STEM image (Fig. 9) shows a clustering effect where ytterbium ions are distributed in the lattice by groups of two or three. The number of atomic columns with 2 or more ytterbium ions exceeds the number predicted by a random distribution of ytterbium ions in the lattice. Therefore, it is clear that ytterbium ions form clusters within the CaF_2 lattice, but the resolution of the HAADF technique does not allow us to identify the types of clusters present (dimers, trimers, hexamers, etc.). In a thermodynamic modeling of defect chemistry in CaF_2, Catlow et al. predicted that Yb^{3+} and other rare earth ions would preferentially form defect clusters, and our analysis of the HAADF images is, therefore, in good agreement with the ytterbium clusters predicted in by Catlow et al.[26]

The HAADF-STEM mode does not allow to reach the vertical position of the ytterbium ions in the columns. A more detailed investigation of the clusters can be performed by optimizing the imaging conditions. The first optimization has already been done by isolating the potential clusters in a diluted 0.5 at% powder. A second optimization is possible by choosing particles with the right zone axes orientation. The Cs corrected-STEM has a field depth of 4 nm,[30] equivalent in CaF_2 to the distance separating 4, 7 or 10 atoms for [1 1 1], [1 0 0] and [1 1 0] zone axis respectively. Indeed, as a function of the orientation, the number of atoms in the field depth of the instrument can be decreased from 10 for the presented images to 4 for [1 1 1] zone axis image. Unfortunately, only a few particles presented this orientation.

It is important to consider whether Yb^{3+} clusters will have any effect on the real in-line transmission (RIT) of the samples:[55]

$$\mathrm{RIT} = (1 - R_s)\exp(-\gamma\varepsilon) \tag{7}$$

where ε is the sample thickness, γ is the scattering coefficient of the material, R_s is the reflection loss at the two sample surfaces at normal incidence:[55]

$$R_s = \frac{2((n-1)/(n+1))^2}{1 + ((n-1)/(n+1))^2} \tag{8}$$

where n is the CaF_2 refractive index. γ is a summation of contributions from all scattering sources in the material (pores, grain boundaries, Yb^{3+} clusters, etc.):[56]

$$\gamma = \gamma_{\mathrm{pores}} + \gamma_{\mathrm{gb}} + \gamma_{\mathrm{Yb\ clusters}} + \cdots \tag{9}$$

where each scattering coefficient is the product of the number of scatterers per unit volume (N) and the scattering cross section of each scatterer, C_{sca}:[56]

$$\gamma = NC_{\mathrm{sca}} \tag{10}$$

If we consider hexamer clusters, which have been identified in single crystal Yb:CaF_2 as the primary cluster type, the average cluster will have a unit cell with lateral dimensions of approximately 0.6 nm. We also assume that the refractive index will be similar to that of YbF_3 (1.56 at 500 nm). To calculate C_{sca} for these clusters, we approximate the shape of the clusters as spheres and use the Rayleigh approximation:

$$C_{\mathrm{sca}} = \frac{256\pi^5}{3}\frac{r^6 n^4}{\lambda^4}\left(\frac{m^2-1}{m^2+2}\right)^2 \tag{11}$$

where r is the cluster radius, λ is the wavelength of the incident light in vacuum, n is the CaF_2 refractive index, and $m = n_{\mathrm{cluster}}/n$ where n_{cluster} is the refractive index of the hexamer cluster. The Rayleigh approximation is valid when $r < \lambda/40$ and $4m\pi nr/\lambda \ll 1$.[56] For an incident wavelength of 500 nm and approximating the hexamer clusters as 0.6 nm diameter spheres with the same refractive index as YbF_3 (1.56), both criteria for the Rayleigh criteria are valid (0.3 nm < 12.5 nm, and $0.012 \ll 1$). For these conditions, C_{sca} is calculated to be $4.52 \times 10^{-26}\,\mathrm{cm}^2$. For a 10 at% Yb:$CaF_2$ sample with, 0.1 cm thickness, and assuming all of the Yb^{3+} forms hexamer clusters, the total loss due to the clusters is 1.85×10^{-4}%. It is important to note that this value is an upper bound for the possible scattering, and thus, the presence of Yb^{3+} clusters has a negligible effect on the transparency of the samples.

4. Conclusions

We present here the best known ytterbium doped calcium fluoride transparent ceramic using a soft chemistry route for the powder synthesis. The optical losses in our material are low, $0.16\,\mathrm{cm}^{-1}$ at 1200 nm, but yet not sufficient to obtain an efficient laser effect. Scanning transmission electron microscopy using the HAADF mode has shown that these losses are induced by defects located at the grain boundaries. Two types of defects have been identified, ytterbium segregation and oxygenized secondary phase.

The grain boundaries with ytterbium segregation do not present secondary phases even if the ytterbium concentration increases up to 9 at%, instead of 6.4 at%, where the grain boundary is almost perfect. The calculated reflectance of this type of grain boundary is very low (0.0004%) and cannot be considered as a major scattering source whereas the oxygenized grain boundaries is the major scattering source. Indeed, the refractive index of a pure calcium oxide secondary phase is very different to the one of calcium fluoride (1.871 and 1.434 respectively) leading to a reflectance of 1.6% and can induce the absorption band at 220 nm (charge transfer band Yb–O).

In addition, this work has shown that the synthesized particles are surrounded by an oxygenized shell which has an inhomogeneous thickness on each particle. The synthesis protocol will be modified in order to tentatively improve the quality of our ceramics by suppressing this shell.

Also, a non-random distribution of the ytterbium ions in the lattice has been observed for the first time. A more precise study will be presented in a forthcoming paper.

Acknowledgements

This study is supported by the DGA.

We thank David Troadec at the IEMN of Lille (France) for the preparation of ceramic thin sections by FIB. Adam Stevenson is acknowledged for fruitful discussion and for scattering calculations.

References

1. Mortier M, Vivien D. Ceramic and glass–ceramic lasers. *Ann Chim Sci Mater* 2003;**28**:21–33.
2. Ikesue A, Kinoshita T, Kamata K, Yoshida K. Fabrication and optical properties of high-performance polycrystalline, Nd:YAG ceramics for solid-state lasers. *J Am Ceram Soc* 1995;**78**:1033–40.
3. Lu J, Ueda KI, Yagi H, Yanagitani T, Akiyama Y, Kaminskii AA. Neodymium doped yttrium aluminum garnet ($Y_3Al_5O_{12}$) nanocrystalline ceramics – a new generation of solid state laser and optical materials. *J Alloys Compd* 2002;**341**:220–5.
4. Soules TF. *Communication*, 3rd LCS Paris, October 8–11; **2007**.
5. Tsunekane M, Taira T. High-power operation of diode edge-pumped, composite all-ceramic Yb:$Y_3Al_5O_{12}$ microchip laser. *Appl Phys Lett* 2007;**90**:121101.
6. Petit V, Camy P, Doualan J, Moncorgé R. CW and tunable laser operation of Yb^{3+} in Nd:Yb:CaF_2. *Appl Phys Lett* 2006;**88**:51111.
7. Slack G, Oliver D, Chrenko R, Robert S. Optical absorption of $Y_3Al_5O_{12}$ from 10 to 55 000-cm^{-1} wave numbers. *Phys Rev* 1969;**177**: 1308–14.
8. Malitson IH. A redetermination of some optical properties of calcium fluoride. *Appl Opt* 1963;**2**:1103–7.
9. Boudeile J, Didierjean J, Camy P, Doualan JL, Benaya A, Ménard V, et al. Thermal behaviour of ytterbium-doped fluorite crystals under high power pumping. *Opt Express* 2008;**16**:10098–109.
10. Kaminskii AA. *Laser crystals*. 2nd revised ed. Springer-Verlag; 1990.
11. Siebold M, Bock S, Schramm U, Xu B, Doualan JL, Camy P, et al. Yb:CaF_2 – a new old laser crystal. *Appl Phys B* 2009;**97**:327–38.
12. Bensalah A, Mortier M, Patriarche G, Gredin P, Vivien D. Synthesis and optical characterizations of undoped and rare-earth-doped CaF_2 nanoparticles. *J Solid State Chem* 2006;**179**:2636–44.
13. Aubry P, Bensalah A, Gredin P, Patriarche G, Vivien D, Mortier M. Synthesis and optical characterizations of Yb-doped CaF_2 ceramics. *Opt Mater* 2009;**31**:750–3.
14. Petit V, Doualan JL, Camy P, Moncorgé R, Menard V. CW and tunable laser operation of Yb^{3+} doped CaF_2. *Appl Phys B* 2004;**78**:681–4.
15. Lucca A, Debourg G, Jacquemet M, Druon F, Balembois F, Georges P, et al. High-power diode-pumped Yb^{3+}:CaF_2 femtosecond laser. *Opt Lett* 2004;**29**:2767–9.
16. Su L, Xu J, Xue Y, Wang C, Chai L, Xu X, et al. Low-threshold diode-pumped Yb^{3+},Na^{+}:CaF_2 self-Q-switched laser. *Opt Express* 2005;**13**:348–52.
17. Siebold M, Hornung M, Bock S, Hein J, Kaluza MC, Wemans J, et al. Broad-band regenerative laser amplification in ytterbium-doped calcium fluoride (Yb:CaF_2). *Appl Phys B* 2007;**89**:543–7.
18. Basiev TT, Doroshenko ME, Fedorov PP, Konyushkin VA, Kuznetsov SV, Osiko VVSh, et al. Efficient laser based on CaF_2–SrF_2–YbF_3 nanoceramics. *Opt Lett* 2008;**33**:521–3.
19. Hatch SE, Parsons WF, Weagley RJ. Hot-pressed polycrystalline CaF_2:Dy^{2+} laser. *Appl Phys Lett* 1964;**5**:153–4.
20. Ramirez MO, Wisdom J, Li H, Aung YL, Stitt J, Messing GL, et al. Three-dimensional grain boundary spectroscopy in transparent high power ceramic laser materials. *Opt Express* 2008;**16**:5965–73.
21. Zhao W, Mancini C, Amans D, Boulon G, Epicier T, Min Y, et al. Evidence of the inhomogeneous Ce^{3+} distribution across grain boundaries in transparent polycrystalline Ce^{3+}-doped $(Gd,Y)_3Al_5O_{12}$ garnet optical ceramics. *Jpn J Appl Phys* 2010;**49**:022602.
22. Kueck AM, Kim DK, Ramasse QM, De Jonghe LC, Ritchie RO. Atomic-resolution imaging of the nanoscale origin of toughness in rare-earth doped SiC. *Nano Lett* 2008;**8**:2935–9.
23. Ziegler A, Idrobo JC, Cinibulk MK, Kisielowski C, Browning ND, Ritchie RO. Interface structure and atomic bonding characteristics in silicon nitride ceramics. *Science* 2004;**306**:1768–70.
24. Winkelman GB, Dwyer C, Hudson TS, Nguyen-Manh D, Doblinger M, Satet RL, et al. Three-dimensional organization of rare-earth atoms at grain boundaries in silicon nitride. *Appl Phys Lett* 2005;**87**:061911.
25. Corish J, Catlow C, Jacobs P, Ong S. Defect aggregation in anion-excess fluorites. Dopant monomers and dimers. *Phys Rev B* 1982;**25**:6425–38.
26. Bendall PJ, Catlow CRA, Corish J, Jacobs PWM. Defect aggregation in anion-excess fluorites more than two impurity atoms II. Clusters containing. *J Solid State Chem* 1984;**51**:159–69.
27. Petit V, Doualan JL, Camy P, Portier X, Moncorgé R. Spectroscopy of Yb^{3+}:CaF_2: from isolated centers to clusters. *Phys Rev B* 2008;**78**:1–12.
28. Sobolev BP, Fedorov PP, Seiranian KB, Tkachenko NL. On the problem of polymorphism and fusion of lanthanide trifluorides. I. The influence of oxygen on phase transition temperatures. *J Solid State Chem* 1976;**17**:201–12.
29. Karimov DN, Krivandina EA, Zhmurova ZI, Sobolev BP, Bezhanov VA, Chernov SP, et al. Investigation of multicomponent fluoride optical materials in the UV spectral region: I. Single crystals of $Ca_{1-x}R_xF_{2+x}$ (R = Sc, Y, La, Yb, Lu) solid solutions. *Crystallogr Rep* 2006;**51**:1009–15.
30. Borisevich AY, Lupini AR, Travaglini S, Pennycook SJ. Depth sectioning of aligned crystals with the aberration-corrected scanning transmission electron microscope. *J Electron Microsc* 2006;**55**:7–12.
31. Pennycook SJ, Jesson DE. High-resolution Z-contrast imaging of crystals. *Ultramicroscopy* 1991;**37**:14–38.
32. Pennycook SJ, Jesson DE. High-resolution incoherent imaging of crystals. *Phys Rev Lett* 1990;**64**:938–42.
33. Kaiser W, Spitzer W, Kaiser R, Howarth L. Infrared properties of CaF_2, SrF_2, and BaF_2. *Phys Rev* 1962;**127**:1950–4.
34. Boulon G, Lupei V. Energy transfer and cooperative processes in Yb^{3+}-doped cubic sesquioxide laser ceramics and crystals. *J Lumin* 2007;**125**:45–54.
35. Camy P, Doualan JL, Benayad A, von Edlinger M, Ménard V, Moncorgé R. Comparative spectroscopic and laser properties of Yb^{3+}-doped CaF_2, SrF_2 and BaF_2 single crystals. *Appl Phys B* 2007;**89**:539–42.
36. Sua L, Xu J, Li H, Wen L, Yang W, Zhao Z, et al. Crystal growth and spectroscopic characterization of Yb-doped and Yb, Na-codoped CaF_2 laser crystals by TGT. *Cryst Growth* 2005;**277**:264–8.
37. Nicoara I, Pecingina-Garjoaba N, Bunoiu OJ. Crystal growth and spectroscopic characterization of Yb-doped and Yb, Na-codoped CaF_2 laser crystals by TGT. *Cryst Growth* 2008;**310**:1476–81.
38. Kaczmarek SM, Tsuboi T, Ito M, Boulon G, Leniec G. Optical study of Yb^{3+}/Yb^{2+} conversion in CaF_2 crystals. *J Phys Condens Matter* 2005;**17**:3771–86.
39. Doualan JL, Camy P, Benayad A, Ménard V, Moncorgé R, Boudeile J, et al. Yb^{3+} doped (Ca,Sr,Ba)F_2 for high power laser applications. *Laser Phys* 2009;**20**:533–6.
40. Greskovich C, Chernoch JP. Polycristalline ceramics lasers. *J Appl Phys* 1973;**44**:4599–606.
41. Aschauer U, Bowen P, Parker SC. Surface and mirror twin grain boundary segregation in Nd:YAG: an atomistic simulation study. *J Am Ceram Soc* 2008;**91**:2698–705.
42. Aschauer U. *Thesis*. Lausanne, Switzerland: Ecole Polytechnique Fédérale de Lausanne; **2008**.
43. Nordstrom D, Jenne E. Fluorite solubility equilibria in selected geothermal waters. *Geochim Cosmochim Acta* 1977;**41**:175–88.
44. Glasson DR. The production of active solids by thermal decomposition. Part VIII: calcination of calcium hydroxide. *J Chem Soc* 1956:1506–10.
45. Dillon SJ, Tang M, Carter WC, Harmer MP. Complexion: a new concept for kinetic engineering in materials science. *Acta Mater* 2007;**55**:6208–18.
46. Gladstone JH, Dale TP. Researches on the refraction, dispersion and sensitiveness of liquid. *Philos Trans R Soc* 1863;**153**:317–43.
47. Larsen ES, Berman H. *The microscopic determination of the nonopaque minerals*. Geological Survey Bulletin Unite States Department of the Interior; 1934. p. 848.

48. Jaffe HW. Application of the rule of gladstone and dale to minerals. *Am Mineral* 1956;**41**:757–77.
49. Pauly H. Gladstone-Dale calculations applied to fluorides. *Can Mineral* 1982;**20**:593–600.
50. Database from Nivo Technologies company.
51. Liu CJ. Refractive index of calcium oxide. *J Appl Phys* 1966;**37**:2450–2.
52. Pidol L, Viana B, Galtayries A, Dorenbos P. Energy levels of lanthanide ions in a $Lu_2Si_2O_7$ host. *Phys Rev B* 2005;**72**:125110.
53. Rubloff G. Far-ultraviolet reflectance spectra and the electronic structure of ionic crystals. *Phys Rev B* 1972;**5**:662–84.
54. Whited RC, Flaten CJ, Walker WC. Exciton thermoreflectance of MgO and CaO. *Solid State Commun* 1973;**13**:1903–5.
55. Apetz R, van Bruggen MPB. Transparent alumina A: a light-scattering model. *J Am Ceram Soc* 2003;**86**:480–6.
56. van de Hulst HC. *Light scattering by small particles*. NewYork: Dover; 1982.